Electrically Small, Low-Profile, Full-Duplex Huygens Dipole Filtenna

Zhentian Wu[1], Ming-Chun Tang[1], and Richard W. Ziolkowski[2]

[1]College of Microelectronics and Communication Engineering, Chongqing University, Chongqing 400044, China

[2]Global Big Data Technologies Centre, University of Technology Sydney, Ultimo NSW 2007, Australia

Corresponding author: Ming-Chun Tang

Corresponding author's E-mail: tangmingchun@cqu.edu.cn

Received March 08, 2022

ABSTRACT: An electrically small, low-profile, full-duplex Huygens dipole filtenna is realized as a dense array of two Huygens dipole filtenna (HDF) elements consisting of Egyptian axe dipole and capacitively loaded loop near-field resonant parasitic (NFRP) elements. The dual-band HDF elements operate at two very nearby frequency bands and are physically separated by only 0.12 λ_{LB}. A prototype was fabricated and tested. Benefitting from the HDF element's good out-of-band rejection performance characteristics, high isolation levels between the lower-band (LB) and higher-band (HB) ports are obtained without any decoupling structure. The measured results, in good agreement with their simulated values, demonstrate that the entire system is electrically small (ka = 0.975) and low-profile (0.041 λ_{LB}). The measured isolation levels at its LB and HB ports are, respectively, over 33.9 and 29.2 dB. When the LB port (HB port) is excited, its fractional bandwidth, broadside realized gain, front-to-back ratio, and overall efficiency values are, respectively, 0.86% (0.77%), 2.1 dBi (2.31 dBi), 8.1 dB (9.6 dB), and 62.1% (62.8%).

Key words: Dual-band, electrically small antennas, filtennas, full-duplex, Huygens dipole antennas, low profile

1. INTRODUCTION

Electrically small Huygens dipole antennas (HDAs) have received increased attention in recent years because of their excellent directional radiation performance characteristics. For example, they can exhibit large front-to-back ratios (FTBRs) and wide beamwidths without the requirement of a ground plane [1]. A variety of electrically small HDAs have been reported to date with applications-relevant features, e.g., linearly (LP) [2]–[7] and circularly [8]–[10] polarized designs, reconfigurable designs [11], and non-Foster designs [12]. Another noteworthy advance

has been the development of dual-band full-duplex antennas that operate independently over different bands on a common wireless communications platform with very low mutual interference [13]–[14]. They have been developed in a variety of applications including for use in intelligent transport systems [13] and integrated radio frequency frontends [14]. Consequently, it is expected that if two electrically small HDAs operating at different frequency bands could be combined into an electrically small system with dual-band full-duplex operation, it would be in high demand for many advanced land, sea, air and space based applications [15].

One extremely important feature that must be attained in any full-duplex system is an exceptionally high isolation between its transmission (TX) and reception (RX) ports. For example, band-pass filtennas have been used to suppress the mutual coupling in a dual-band full-duplex system without relying on decoupling elements placed between its TX and RX subsystems [16]. They significantly decreased the design complexity and the cost of the overall system. Several effective methods have been developed to realize the out-of-band rejection functions of filtennas. These include etching long rectangle slots in their ground planes [17], [18]; employing multimode resonators [19]; and utilizing filter synthesis [14], [20]. Unfortunately, they all have undesirable features, e.g., the requirement of large ground planes [17] or the need for many resonators [14], [20]. Consequently, they are not suitable for electrically small, dual-band full-duplex system designs, particularly when a ground plane is undesirable.

In this paper, an innovative finger-based interdigital capacitor (FIDC) structure is engineered to be seamlessly integrated into the near-field resonant parasitic (NFRP) elements of a dual-band HDA. Each HDA is a modification of the successful design reported in [21]. The resulting system has high isolation between its two ports, while maintaining the HDAs' good directional radiation

performance characteristics and its electrically small package. It will be demonstrated that it is an ideal candidate for dual-band full-duplex applications in space limited platforms. All of the numerical simulations and their optimization that are reported herein were performed using the finite-element-based, frequency domain ANSYS/ANSOFT high-frequency structure simulator (HFSS), version 20.0.

2. DUAL-BAND HDF-BASED Full-DUPLEX DESIGN

The antenna's configuration is shown in Fig. 1. Its optimized design parameters are given in Table I. It consists of four substrate layers which all have the same radius, $R1$ = 36.5 mm, and the same 0.035 mm thickness. Layer_1, Layer_2 and Layer_3 are Taconic TLY-5 copper-cladded substrates (relative dielectric constant ε_r = 2.2, loss tangent tan δ = 0.0009). Layer_4 is a Rogers Diclad 880 copper-cladded substrate (relative dielectric constant ε_r = 2.2, loss tangent tan δ = 0.0009). They are supported with four 3D printed brackets. Our simulation studies indicated that these brackets have little impact on the antenna performance.

As shown in Fig. 1, the magnetic elements are two different size capacitively loaded loops (CLLs). The horizontal portions of these CLLs are printed on the upper surfaces of Layer_2 and Layer_4. They are connected by four cylindrical copper columns whose heights and radii are, respectively, h6 and R8. These four columns pass completely through Layer_3, as shown in Fig. 1(b). Fig. 1(c) shows each CLL integrated with two pairs of FIDCs, which are placed on the upper surface of Layer_1. These FIDC strips are connected to the CLLs by a via with radius R2 that passes through Layer_1. The two electric NFRP elements are, respectively, two Egyptian axe dipoles (EAD) printed on the upper surface of Layer_3, as shown in Fig. 1(e). Two copper rings

that have an inner radius *R6* > *R8* are integrated into the main strip of the EAD. The four copper cylindrical columns of the CLLs pass completely through Layer_3 within them. This arrangement avoids the magnetic elements being shorted to the EADs.

Several design details must be elucidated. As shown in Fig. 1, the longer and shorter FIDC-based CLL NFRP elements are placed on opposite sides of the centerline of the substrates and are oriented parallel to the x-axis. The distances from the centerline to the edges of these FIDC-based CLLs are *g5* and *g6*, respectively. Thus, the center-to-center distance of the two elements is only 0.12 λ_{LB}, i.e., the two-element array is densely packed. Because of their different sizes, we denote port 1 (port 2) as the source that excites the longer (shorter) CLL-EAD pair. Both pairs radiate a broadside Huygens LP field that is polarized both along the x-axis and whose maximum is pointed along the +z-axis. Note that the two additional parasitic rectangular copper strips shown in Fig. 1(d) are located on the upper surface of Layer_2. They have different lengths and widths, i.e., *L7* ≠ *L8* and *W4* ≠ *W5*. The distances between the nearest edges of the CLLs and these strips are *g4* and *g7*. As will be demonstrated in Section 4, their presence helps to improve the H-plane realized gain (RG) patterns of the two ports.

The integration of the two pairs of FIDCs with the CLL NFRP element empowers the good out-of-band rejection performance of the HDF design. The corresponding simulated performance characteristics of the FIDC-based CLL NFRP antenna are shown in Fig. 2. The first FDIC pair (highlighted in red) is integrated on the top of the CLL element to produce a deep radiation null at the lower frequency out of the bandwidth, i.e., at 1.2 GHz. Furthermore, the second FDIC pair (highlighted in blue) is placed symmetrically on the outside of the first pair to create an additional radiation null at

1.43 GHz near the higher band edge. Note that the FIDCs, which facilitate the creation of these radiation nulls, have been described in [21]. Those particular details will not be repeated here.

3. SIMULATED AND MEASURED RESULTS

The optimized electrically small, dual-band, HDF-based full-duplex system was fabricated, assembled and measured. The assembled system was mounted on two 50-Ω coaxial cables, the one connected to port 1 (port 2) is 57.5 mm (52.4 mm), as shown in Fig. 3(a). The baluns mitigated any spurious currents induced on the outer walls of the long coax cables and ensured the accuracy of the measurements of the S-parameters and RG patterns [22]. We emphasize that the baluns were only ancillary to the measurements. The far-field radiation performance characteristics of the developed full-duplex system were measured with an SG128 multi-probe antenna measurement system. The antenna under test (AUT) in this chamber is shown in Fig. 3(b).

The measured and simulated (taking into account the presence of both baluns) performance characteristics of the prototype system are presented in Figs. 4 and 5. As shown in Fig. 4, the measured (simulated) resonance frequencies for port 1 and port 2 are 1.276 (1.28) GHz and 1.434 (1.44) GHz, respectively, where $|S_{11}|_{min}$ = –16.3 (–14.2) dB and $|S_{22}|_{min}$ = –24.1 (–27.3) dB. The measured –10-dB bandwidths are 11.0 MHz, from 1.272 to 1.283 GHz (0.86%) and 11.0 MHz, from 1.428 to 1.439 GHz (0.77%) for the LB and HB, respectively. The simulated boresight realized gain values indicate that the left CLL-EAD pair generates a radiation null in the HB (i.e., at 1.44 GHz) and the right CLL-EAD pair generates a radiation null in the LB (i.e., at 1.3 GHz). Therefore, high isolation levels between the LB and HB ports are obtained. The measured (simulated) isolation in the LB is higher than 33.9 (34.1) dB, and that in the HB is higher than 29.2 (30.2) dB. The corresponding measured (simulated) electrical size and total height of the

system at the lower operating frequency are ka = 0.975 (0.978) and 0.041 λ_{LB} (0.041 λ_{LB}), respectively. These measured results are in good agreement with their simulated values, confirming that the mutual coupling of the dual-band HDF-based full-duplex system was suppressed even with the dense placement of its two HDF elements and their shared dielectric disks. In fact, it is witnessed that the isolation between the ports of our design has been significantly improved with the FIDC structures, i.e., without them the simulated isolation is only -24 and -19.6 dB, respectively, in the LB and HB.

The measured and simulated RG patterns are given in Fig. 5. Clearly, good broadside radiation performance and reasonable cardioid patterns were obtained as expected [6]. The main-beam direction when each port is independently excited is strictly pointed along the +z-axis. When port 1 was excited while port 2 was terminated with a 50-Ω load, the measured (simulated) peak RG, FTBR, and overall efficiency (OE) values at 1.276 (1.28 GHz) were 2.1 (2.5) dBi, 8.1 (10) dB, and 62.1% (65.6%), respectively. The half-power beamwidths were 107°, from -55° to 52° (112°, from -56° to 56°) in the E-plane (z0x plane) and 155°, from -84° to 71° (171°, from -85° to 86°) in the H-plane (z0y plane). Similarly, when port 2 was excited, the measured (simulated) peak RG, FTBR, and OE values at 1.434 (1.44 GHz) were 2.31 (2.77) dBi, 9.6 (11.5) dB, and 62.8% (66%), respectively. The half-power beamwidths were 111°, from -54° to 57° (120°, from -59° to 61°) in the E-plane (z0x plane) and 146°, from -70° to 76° (160°, from -75° to 85°) in the H-plane (z0y plane). The measured (simulated) maximum cross-polarization levels were -30.76 (-41.35) dB for the LB and -30.8 (-39.77) dB for the HB, respectively. Both outcomes demonstrate high polarization purity within each operating frequency band.

4. OPERATING MECHANISMS

The impact of the rectangular copper strips on the RG patterns in both frequency bands was examined. Fig. 6 shows the simulated S-parameters, along with the 3-D directivity patterns at the resonance frequencies of both ports without them being present. First, compared with the simulated results presented in Fig. 4, the presence of the parasitic copper strips has essentially no impact on the isolation level between the two ports. Second, one observes that there is a degradation of the RG patterns, especially at the HB, when the parasitic copper strips are not present. When only port 1 (port 2) is excited, this degradation is particularly noticeable in the H-plane, where the peak RG pattern deviates significantly from the +z-axis by approximately 6° (20°), as indicated in Fig. 5.

In order to illustrate the operating mechanisms of the parasitic copper strips, we use the case when port 2 is excited. The current distributions on the main metallic surfaces with and without the parasitic copper strips are presented and compared at the resonance frequency 1.44 GHz in Fig. 7. The currents distributions on the driven dipoles and on the upper surfaces of the FIDC-based CLL and the EAD elements are highlighted at the times 0, T/4, T/2, and 3T/4, where T is the corresponding source period. The additional solid red (referring to the elements of port 2) and dotted purple (referring to the elements of port 1) arrows annotate their directional behavior for visual convenience.

When only port 2 is excited, the majority of the surface currents are distributed on the elements directly associated with port 2 as expected. Referring to the current behavior analysis of the HDA reported in [4], the variation of the red arrows on the right CLL and EAD NFRP pair over the entire period indicates that they are resonant and their current moments are in-phase. The

indicated current directions generate the Huygens cardioid RG patterns whose maxima are directed along the +z-axis [4]. One finds in Figs. 7(a) and 7(b) that there are relatively weak surface current distributions on the left CLL-EAD pair induced by the field radiated by the right one, but there is almost no current on the dipole element terminated at port 1. The reason for this behavior is that the left CLL-EAD pair generates a radiation null in the HB that rejects the incident power at those frequencies. It accounts for the high port-to-port isolation when the system operates in the HB.

On the other hand, because the FIDC-loaded CLL elements are in parallel and placed close to each other, the weak currents on the left (passive) CLL do impact the symmetry of the right (active) one's RG patterns as shown in Fig. 6. Moreover, since the left CLL is longer than the right one, it acts as a "reflector" while the right one acts as the "driven element" in a quasi-Yagi configuration. Therefore, in the absence of the parasitic strips, a tilt of the directivity pattern in the H-plane (z0y plane) away from the +z-axis toward the +y-axis occurs. In contrast, when they are present, the induced currents on the right parasitic copper strip are in phase with the right CLL element over the entire period. By optimizing its total length and width, the effects of the out-of-phase current on the left CLL surface are canceled out and the strictly broadside pattern shown in Fig. 5(b) is obtained. Likewise, when port 1 is excited, similar current behaviors are obtained.

To understand the efficacy of our developed electrically small, dual-band, HDF-based full-duplex system, fair comparisons of its prototype's performance and several recently reported dual-band, full-duplex antennas are given in Table II. It is a comprehensive list of the values of the

electrical sizes, bandwidths, RG values, FTBR values, isolation levels, frequency ratio values, and ground-dependent features.

Two dual-band, full-duplex antennas were reported in [17] and [18]. The volumes of the two antennas were, respectively, 0.97 × 10-2 λ_{LB}^3 (ka = 4.5) [17] and 0.5 × 10-2 λ_{LB}^3 (ka = 2.54) [18]. The isolation level in the LB was higher than 20.3 dB in [17] and 21.0 dB in [18]. It was higher than 23.0 dB and 28.0 dB, respectively, in the HB. In contrast, the volume of our antenna, 0.28 × 10-2 λ_{LB}^3, is 3.46 times smaller than that in [17] and 1.78 times smaller than that in [18]. The isolation levels of our antenna in the LB and HB are over 33.9 dB and 29.2 dB, respectively, which are significantly better than those in [17] and [18]. Moreover, the physical aperture area of our antenna, 7 × 10-2 λ_{LB}^2, is 13.92 times smaller than that in [17] and 4.57 times smaller than that in [18]. Despite its much smaller size, the RG values of our antenna are only ~2.72 times smaller than those in [17] and ~1.56 times smaller than those in [18]. In addition, the isolation levels of the antennas in [13], [14] are comparable to ours, but they all required a larger volume to achieve those values. Furthermore, Table II highlights the fact that our full-duplex system achieves its isolation levels without a ground plane and that the frequency ratio f_{HB}/f_{LB} is one of the smallest. Its low fractional bandwidths in comparison to all of the comparison antennas are a direct consequence of this feature.

5. CONCLUSION

An electrically small, low-profile, dual-band, HDF-based full-duplex design, its design features and its performance characteristics were reported. It is a dense array consisting of two Huygens dipole filtennas and two parasitic strips to rebalance its RG patterns to have their maxima along the broadside

direction. The distance between the elements is only $0.12\lambda_{LB}$. A prototype of the developed full-duplex system was fabricated and tested. The measured results were shown to be in good agreement with their simulated values, confirming that the system suppresses the mutual coupling of the two HDFs operating at different frequency bands without any intervening decoupling structures. The measured isolation levels in the LB and HB were over 33.9 dB and 29.2 dB, respectively, and the corresponding HB/LB frequency ratio was only 1.12. The RG patterns were cardioid-like with wide beamwidths over both operating bands. Since it is the only electrically small dual-port full-duplex system reported to date, it is a very attractive choice for the many modern space-limited, portable, narrowband wireless platforms that must perform full-duplex operations such as wirelessly powered sensors that require simultaneous wireless communications and power transfer (SWIPT) performance.

Reference

1. S. R. Best, "Progress in the design and realization of an electrically small Huygens source," in Proc. 2010 International Workshop on Antenna Technology (iWAT), Lisbon, 2010, pp. 1-4, Mar. 2010.
2. P. Jin and R. W. Ziolkowski, "Metamaterial-inspired, electrically small, Huygens sources," IEEE Antennas Wireless Propag. Lett., vol. 9, pp. 501-505, May 2010.
3. R. W. Ziolkowski, "Low profile, broadside radiating, electrically small Huygens source antennas," IEEE Access, vol. 3, pp. 2644-2651, Dec. 2015.
4. M.-C. Tang, H. Wang, and R. W. Ziolkowski, "Design and testing of simple, electrically small, low-profile, Huygens source antennas with broadside radiation performance," IEEE Trans. Antennas Propag., vol. 64, no. 11, pp. 4607-4617, Nov. 2016.

5. W. Lin, R. W. Ziolkowski and J. Huang, “Electrically small, low-profile, highly efficient, Huygens dipole rectennas for wirelessly powering internet-of-things devices,” IEEE Trans. Antennas Propag., vol. 67, no. 6, pp. 3670-3679, Jun. 2019.
6. M.-C. Tang, Z. Wu, T. Shi, H. Zeng, W. Lin, and R. W. Ziolkowski, “Dual-linearly polarized, electrically small, low-profile, broadside radiating, Huygens dipole antenna,” IEEE Trans. Antennas Propag., vol. 66, no. 8, pp. 3877–3885, Aug. 2018.
7. S. Lee, G. Shin, S. M. Radha, J. Choi and I. Yoon, “Low-Profile, electrically small planar Huygens source antenna with an endfire radiation characteristic,” IEEE Antennas Wirel. Propag. Lett., vol. 18, no. 3, pp. 412-416, Mar. 2019.
8. P. Alitalo, A. O. Karilainen, T. Niemi, C. R. Simovski, and S. A. Tretyakov, “Design and realisation of an electrically small Huygens source for circular polarisation,” IET Microw., Antennas Propag., vol. 5, no. 7, pp. 783–789, May 2011.
9. W. Lin and R. W. Ziolkowski, “Electrically-small, low-profile, Huygens circularly polarized antenna,” IEEE Trans. Antennas Propag., vol. 66, no. 2, pp. 636-643, Feb. 2018.
10. W. Lin and R. W. Ziolkowski, “Electrically small Huygens CP rectenna with a driven loop element maximizes its wireless power transfer efficiency,” IEEE Trans. Antennas Propag., vol. 68, no. 1, pp. 540-545, Jan. 2020.
11. P. F. Hu, Y. M. Pan and B. Hu, “Electrically small, planar, complementary antenna with reconfigurable frequency,” IEEE Trans. Antennas Propag., vol. 67, no. 8, pp. 5176-5184, Aug. 2019.
12. M.-C. Tang, T. Shi, and R. W. Ziolkowski, “Electrically small, broadside radiating Huygens source antenna augmented with internal non-Foster elements to increase its bandwidth,” IEEE

Antennas Wirel. Propag. Lett., vol. 16, pp. 712-715, 2017.

13. C. Mao, S. Gao and Y. Wang, “Dual-band full-duplex Tx/Rx antennas for vehicular communications,” IEEE Trans. on Veh. Technol., vol. 67, no. 5, pp. 4059-4070, May 2018.
14. C.-X. Mao, S. Gao, Y. Wang, Y. Liu, X.-X. Yang, Z.-Q. Cheng, and Y.-L.Geng, “Integrated dual-band filtering/ duplexing antennas,” IEEE Access, vol. 6, pp. 8403-8411, Feb. 2018.
15. A. H. Abdelrahman and D. S. Filipovic, “Antenna system for full-duplex operation of handheld radios,” IEEE Trans. Antennas Propag., vol. 67, no. 1, pp. 522-530, Jan. 2019.
16. L. Zhao, K. Qian and K. Wu, “A cascaded coupled resonator decoupling network for mitigating interference between two radios in adjacent frequency bands,” IEEE Trans. Microw. Theory Techn., vol. 62, no. 11, pp. 2680-2688, Nov. 2014.
17. Y. Xie, F. Chen and J. Qian, “Design of integrated duplexing and multi-band filtering slot antennas,” IEEE Access, vol. 8, pp. 126119-126126, Jul. 2020.
18. Y. Lee, J. Tarng and S. Chung, “A filtering diplexing antenna for dual-band operation with similar radiation patterns and low cross-polarization levels,” IEEE Antennas Wirel. Propag. Lett., vol. 16, pp. 58-61, 2017.
19. K. Hu, M.-C. Tang, M. Li and R. W. Ziolkowski, “Compact, low-profile, bandwidth-enhanced substrate integrated waveguide filtenna,” IEEE Antennas Wirel. Propag. Lett., vol. 17, no. 8, pp. 1552-1556, Aug. 2018.
20. C. Mao, S. Gao, Y. Wang, F. Qin and Q. Chu, “Compact highly integrated planar duplex antenna for wireless communications,” IEEE Trans. on Microw. Theory and Techn, vol. 64, no. 7, pp. 2006-2013, Jul. 2016.
21. Z. Wu, M. -C. Tang and R. W. Ziolkowski, “Broadside Radiating, Low-Profile, Electrically

Small, Huygens Dipole Filtenna," IEEE Antennas Wirel. Propag. Lett., vol. 21, no. 3, pp. 556-560, Mar. 2022.

22. S. A. Saario, J. W. Lu, and D. V. Thiel, "Full-wave analysis of choking characteristics of sleeve balun on coaxial cables," Electron. Lett., vol. 38, no. 7, pp. 304–305, Mar. 2002.

Footnotes

This work was supported in part by the National Natural Science Foundation of China (contract number 62031006), in part by the Graduate Scientific Research and Innovation Foundation of Chongqing, China (contract number CYB20066), in part by the Chongqing Natural Science Foundation (contract number cstc2019jcyjjqX0004), and in part by the Australian Research Council (grant number DP160102219).

List of Figures

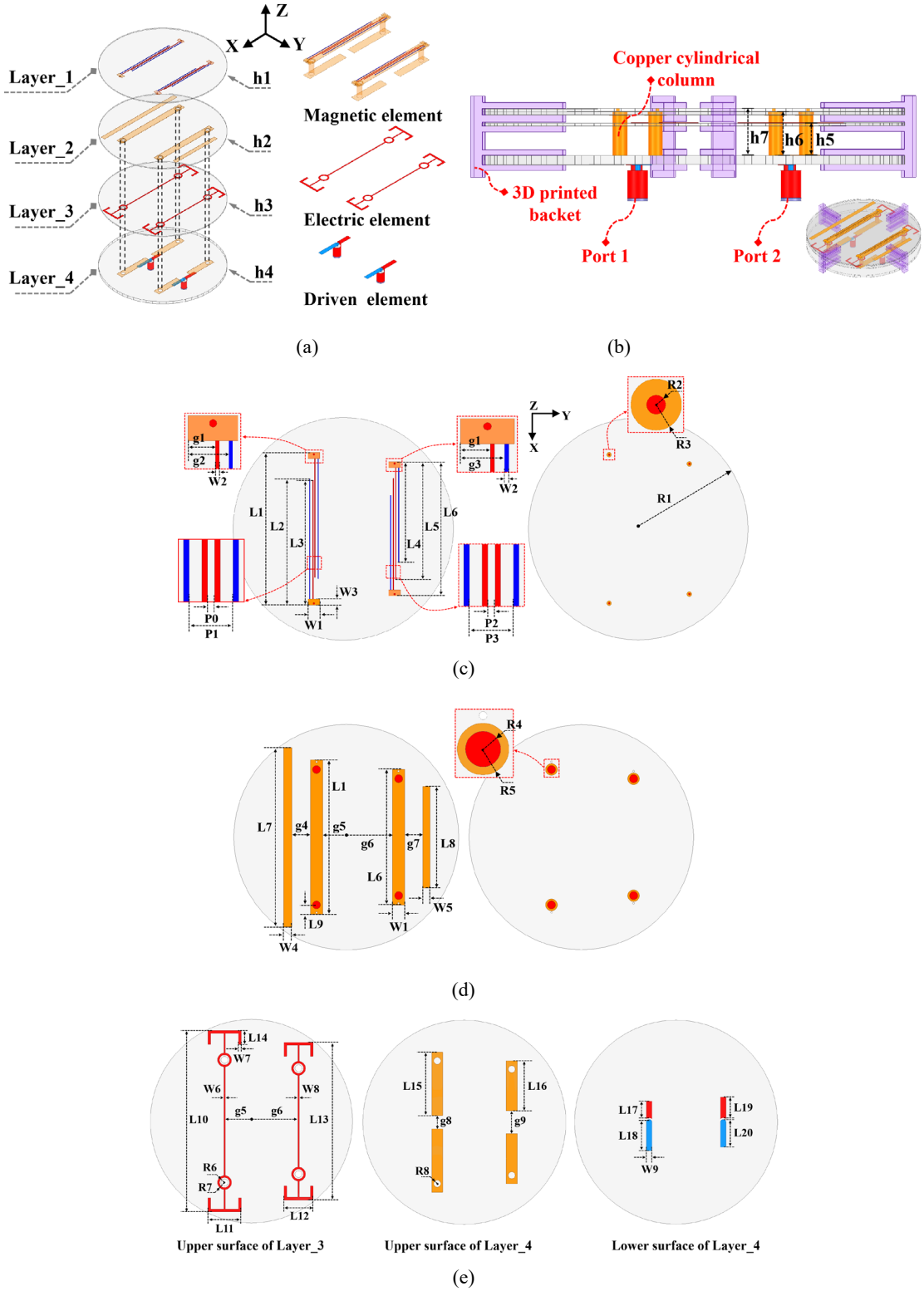

Figure 1. Configuration of the electrically small, HDF-based dual-band full-duplex system. (a) 3-D isometric view. (b) Side view. Upper and lower surfaces of (c) Layer_1, (d) Layer_2. (e) Upper surfaces of Layer_3 and Layer_4 and lower surface of Layer_4.

TABLE I

OPTIMIZED DESIGN PARAMETERS OF THE ELECTRICALLY SMALL, LOW-PROFILE, FULL-DUPLEX HUYGENS DIPOLE FILTENNA (IN MILLIMETERS)

h1=0.508	*h4=1.575*	*h5=5.6*	*h6=7.5*	*h7=8.08*
R1=36.5	*R2=0.3*	*R3=0.8*	*R4=1.3*	*R5=1.9*
R6=1.8	*R7=2.5*	*R8=1.25*	*L1=50.0*	*L2=41.3*
L3=41.0	*L4=33.0*	*L5=38.6*	*L6=44.0*	*L7=58.0*
L8=33.0	*L9=3.0*	*L10=65.0*	*L11=12.0*	*L12=10.5*
L13=56.5	*L14=5.0*	*L15=22.55*	*L16=17.95*	*L17=6.28*
L18=10.2	*L19=7.78*	*L20=9.0*	*W1=4.0*	*W2=0.3*
W3=2.0	*W4=2.5*	*W5=2.4*	*W6=0.524*	*W7=1.0*
W8=0.53	*W9=2.0*	*g1=2.2*	*g2=3.29*	*g3=2.4*
g4=6.05	*g5=7.7*	*g6=15.0*	*g7=5.8*	*g8=4.9*
g9=8.1	*P0=0.4*	*P1=2.58*	*P2=0.4*	*P3=2.4*

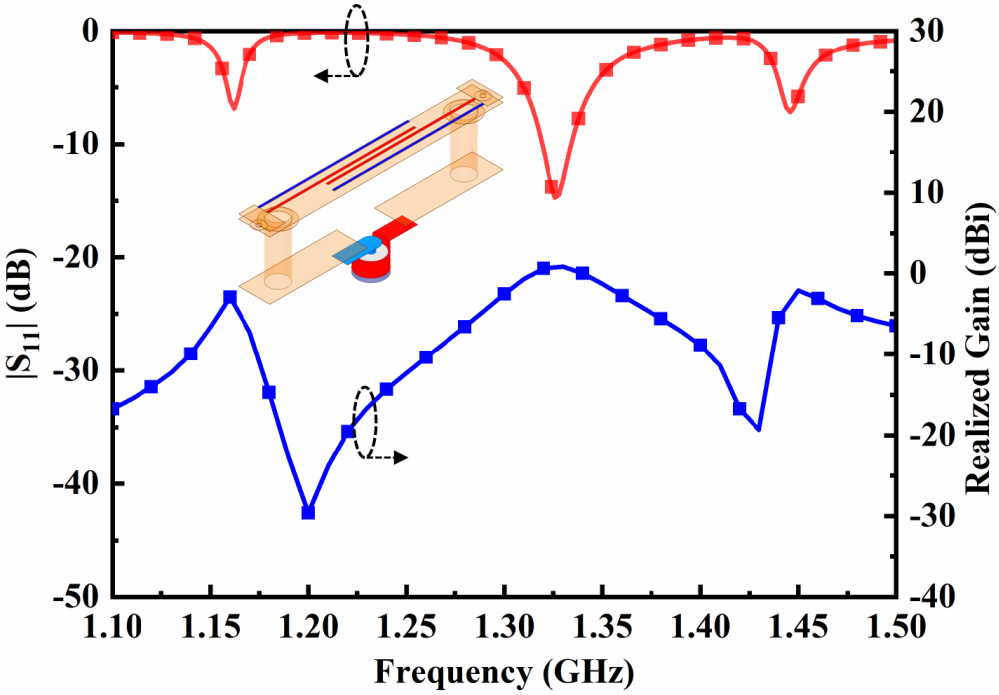

Figure 2. Simulated $|S_{11}|$ and realized gain values of the FIDC-based CLL NFRP antenna.

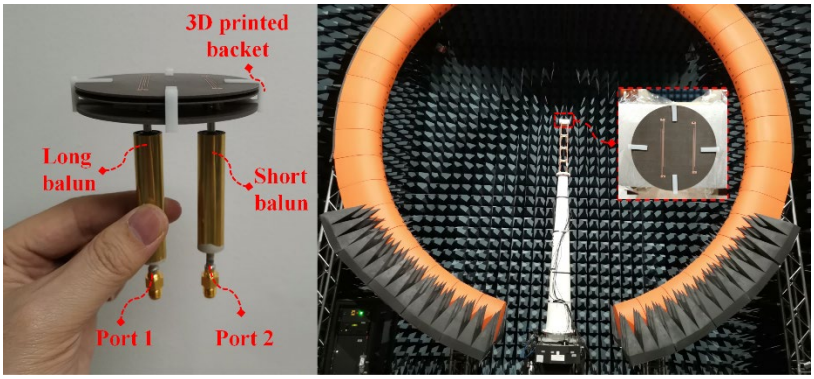

(a) (b)

Figure 3. Fabricated prototype of the electrically small, dual-band, HDF-based full-duplex system. (a) Side view of the assembled system with the two sleeve baluns connected to its ports to ensure accurate measurements. (b) The AUT in the multi-probe anechoic chamber.

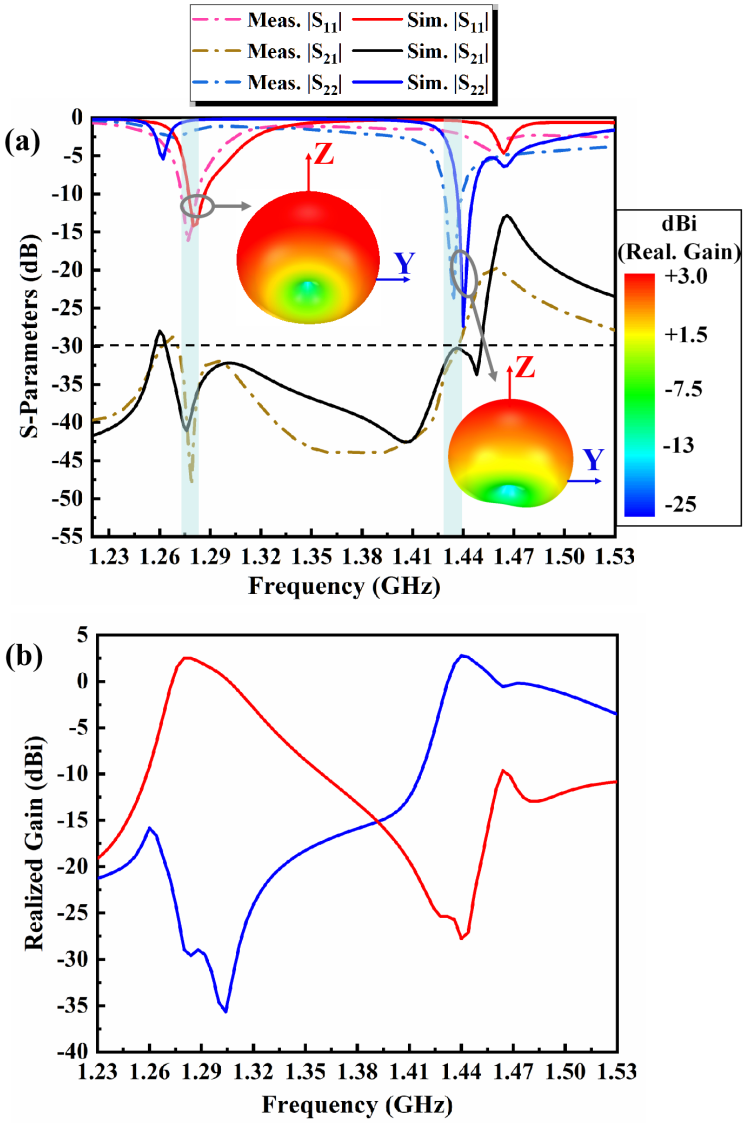

Figure 4. Simulated and measured performance of the electrically small, dual-band, HDF-based full-duplex system. (a) Simulated and measured S-parameters. (b) Simulated realized gain as functions of the source frequency.

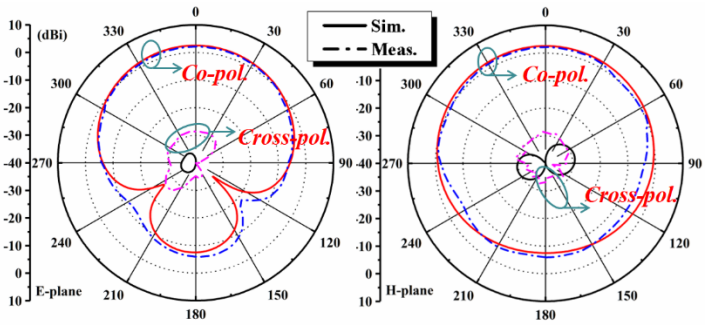

(a)

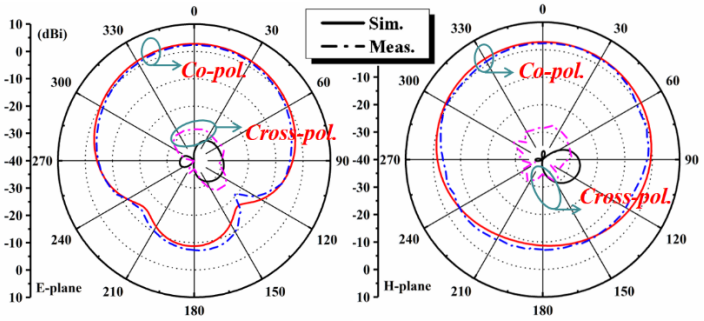

(b)

Figure 5. Measured (simulated) 2-D RG patterns of the electrically small, dual-band, HDF-based full-duplex system. (a) Resonance frequency, 1.276 (1.28) GHz, when port 1 is excited. (b) Resonance frequency, 1.434 (1.44) GHz, when port 2 is excited.

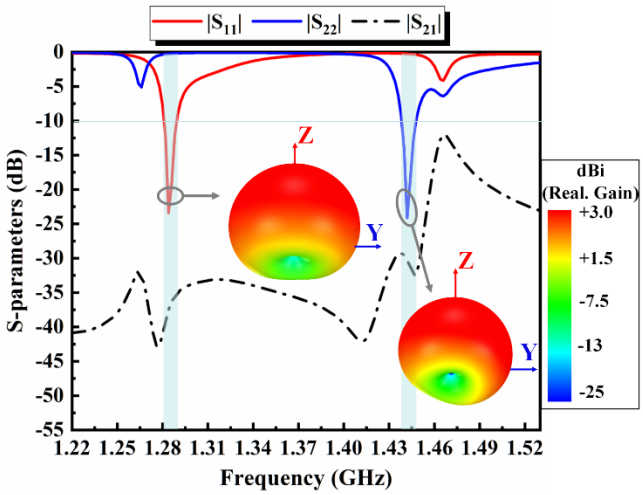

Figure 6. Simulated S-parameters values of the electrically small, dual-band, full-duplex HDA without the rectangular copper parasitic strips being present.

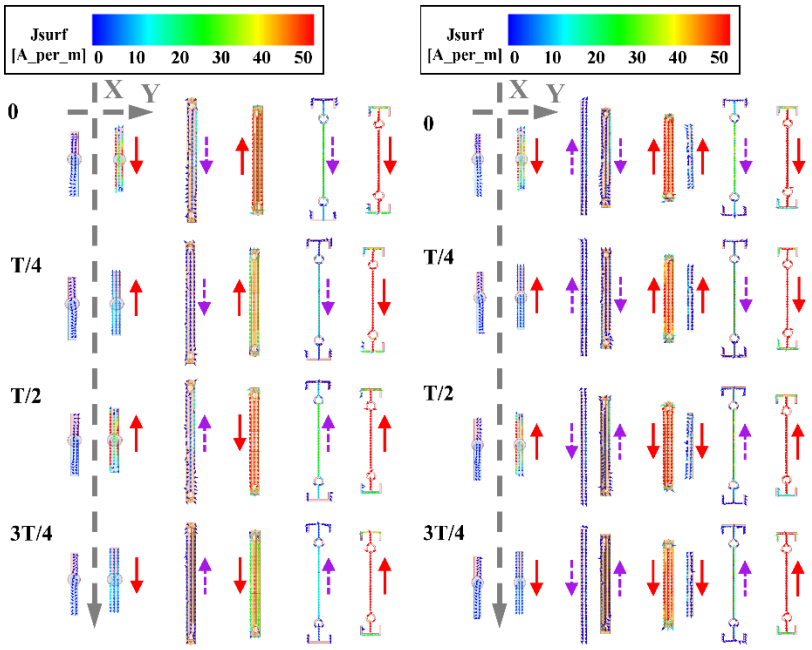

(a) (b)

Figure 7. Surface current distributions on the driven and NFRP elements of the electrically small, dual-band, HDF-based full-duplex system operating in its high frequency band, i.e., with port 2 active and port 1 passive and matched to a 50Ω load. (a) Without the parasitic copper strips being present. (b) With them being present. Left columns: passive and active dipole element, respectively. Center columns: CLL NFRP element. Right columns: EAD NFRP element.

TABLE II

COMPARISON OF THE ELECTRICALLY SMALL, LOW-PROFILE, FULL-DUPLEX HUYGENS DIPOLE FILTENNA WITH RELATED DUAL-BAND, FULL-DUPLEX ANTENNAS REPORTED IN THE LITERATURE

Ref.	ka_{Low}	FBW (%) (LB / HB)	RG (dBi) (LB / HB)	FTBR (dB) (LB / HB)	Isolation (dB) (LB / HB)	Electrical Size (λ_{LB}^3)	Frequency Ratio (f_{HB}/f_{LB})	Ground
[13]	3.49	5.1 / 5.4	6.7 / 8	~27 / ~40	>32 / >30	0.78 × 0.78 × 0.041 = 0.025	1.28	yes
[14]	3.19	5.9 / 5.8	6.5 / 7	~30 / ~28	>30 / >30	0.72 × 0.72 × 0.03 = 0.015	1.38	yes
[17]	4.5	6.3 / 11.5	4.67 / 6.3	~6 / ~7	>20.3 / >23	1.16 × 0.84 × 0.01 = 0.0097	1.49	yes
[18]	2.54	4.5 / 5.5	2.3 / 3.6	- / -	>21 / >28	0.57 × 0.57 × 0.014 = 0.005	2.14	yes
This work	0.975	0.86 / 0.77	2.1 / 2.31	8.1 / 9.6	>33.9 / >29.2	$\pi \times (0.15)^2 \times 0.041$ = 0.0028	1.12	no